Acta Mech 226, 3177–3194 (2015)
DOI 10.1007/s00707-015-1371-x

ORIGINAL PAPER

M. Eynbeygi · M. M. Aghdam

# A micromechanical study on the electro-elastic behavior of piezoelectric fiber-reinforced composites using the element-free Galerkin method

Received: 16 February 2015 / Published online: 13 May 2015


**Abstract** A two-dimensional generalized plane strain micromechanical model is developed to study the electro-elastic behavior of piezoelectric fiber-reinforced composite (PFRC) systems. The composite system consists of long parallel piezoelectric fibers with orthotropic and/or transversely isotropic properties and perfectly bounded to the isotropic matrix in a square array arrangement. In addition, the constituents are assumed to have both linear elastic and electrical behavior, whereas the matrix is piezoelectrically passive. The element-free Galerkin (EFG) method is employed to obtain the solution for the governing system of partial differential equations. The performance of the model is examined for both axial and transverse polarizations and various fiber cross sections. Comparison of the presented results with other techniques available in the literature reveals good agreement. It is demonstrated that the piezoelectric coefficient $e_{31}$ in the transverse polarization is considerably improved in comparison with the corresponding coefficient for pure piezoelectric material. Furthermore, results also show that elliptical fibers may enhance the electrical sensitivity of PFRCs for a specific direction, which is related to the elliptical fiber orientation, in both polarization directions.

## 1 Introduction

Piezoelectric materials are categorized within the intelligent and/or smart materials and usually involve interactions between electrical and mechanical loadings. Due to their special properties to coupled electrical and mechanical energies, they found excellent applications in sensors and actuators. However, there are several concerns related to pure ceramic-based piezoelectric materials, such as low piezoelectric constants, high acoustic impedance, high weight and low ductility. To overcome these limitations in monolithic piezoelectric materials, different types of piezoelectric composites were introduced. Details of various types of PFRCs and their applications can be found elsewhere [1]. A few experimental [2,3], analytical [4–16] and numerical [8,17–19] studies have been proposed to investigate various characteristics of 1–3 piezoelectric composites such as elastic, electric and thermal behavior. Odegard [7] developed a new micromechanical model using a combination of Mori–Tanaka and self-consistent methods to predict the electromechanical properties of piezoelectric polymer composites in axial polarization. In addition, the asymptotic homogenization method (AHM) [4,8,14] has been employed to estimate the overall electro-elastic behavior of axially polarized piezoelectric composites. Apart from the determination of overall electro-elastic coefficients of PFRCs, special attention was given in [8] to establish appropriate boundary conditions (BCs) for the representative volume

M. Eynbeygi · M. M. Aghdam (✉)
Department of Mechanical Engineering, Thermoelasticity Center of Excellence,
Amirkabir University of Technology, Hafez Ave., Tehran, Iran
E-mail: aghdam@aut.ac.ir
Tel.: +98 (21) 6454 3429

M. Eynbeygi
E-mail: Mehdi.eynbeygi@aut.ac.ir

element (RVE) to ensure the periodicity condition using a combination of the AHM and finite element (FE) methods. In the last decade, Mallik and Ray [6], Ray [9] and Kumar and Chakraborty [12] reported a discussion related to the improvement of the effective piezoelectric coefficient $e_{31}$ of unidirectional piezoelectric composites in case they are transversely polarized. Using analytical models, they indicated that the $e_{31}$ piezoelectric coefficient in PFRCs is significantly improved in comparison with a pure piezoelectric material. However, predictions of the analytical models may deviate from reality mainly due to various simplifying assumptions. The finite element micromechanics-based model is developed to predict the overall electro-elastic properties of PFRCs with various fiber shapes [18] and polarization directions of both constituents [17]. Very recently, various orientations of the axis of transverse symmetry were studied on the effective permittivity properties of fiber-reinforced composites, and the explicit formulas were developed using the AHM method [15].

As reviews imply, there are few studies in the literature related to the effects of fiber shape and polarization direction on the electro-elastic properties of PFRCs.

In the present work, a two-dimensional generalized plane strain (GPS) micromechanical model is developed to study the electro-elastic behavior of PFRCs. The EFG method is used to obtain the solution of the coupled electromechanical partial differential equations. Proper discretized forms of periodic BCs and displacement continuity at the fiber and matrix interface in the unit cell model were discussed. The method is used to study the overall electro-elastic properties of PFRCs with circular and elliptical fibers in both axial and transverse polarization directions. An attempt is made to assess some potential benefits by using elliptical fibers. Investigations revealed that the piezoelectric coefficient $e_{31}$ in the PFRCs with transverse polarization is considerably improved in comparison with pure piezoelectric materials. From the overall point of view, it was found that elliptical fibers may enhance the electrical sensitivity of PFRCs for a specific direction in both polarization directions.

## 2 Analysis

### 2.1 Micromechanical model

In a real PFRC, fibers are distributed in a random arrangement. In order to reduce computational cost, similar to most of analytical and numerical micromechanical models, the geometry of the system was simplified by considering unidirectional piezoelectric fibers to be arranged in a square array packing periodically distributed within the matrix. The next step was to consider the smallest and informative repeating area of the geometry as the representative volume element (RVE) for the whole system. In the present study, normal mode sensing and normal mode actuation are assumed. Normal mode sensing occurs when a piezoelectric material is subjected to normal stresses or strains in any of the three spatial directions, which induces an electric field along the polarization direction. Moreover, normal mode actuation occurs when a piezoelectric material is subjected to an electrostatic field parallel to the polarization direction. This causes normal strains in any of the three directions [20]. Therefore, a quarter of piezoelectric fiber surrounded by the corresponding matrix, as shown in Fig. 1, is enough to model the composite behavior. Furthermore, the matrix and fibers are assumed to have linear elastic behavior and are fully bonded to each other. In addition, both constituents of the RVE are assumed to have isotropic and transversely isotropic properties, respectively, while the matrix is supposed to be piezoelectrically passive. Figure 1 also shows a radial nodal distribution within the RVE which is used in this study. As reviews indicated [21], a better accuracy can be found in EFG using a regular distribution of nodes in comparison with irregular ones.

#### *2.1.1 Generalized plane strain (GPS) assumption*

In the micromechanical modeling of composites with long and parallel fibers, the GPS is an appropriate assumption for the analysis of fibrous composites. As shown in Fig. 1, the $x_3$ axis is parallel to the fiber direction, while the $x_1 - x_2$ axes are oriented in the transverse directions. The $x_1 - x_2$ is a plane of symmetry which means both stress and strain fields are invariant with respect to the longitudinal axis. Furthermore, based on the GPS assumptions, the strain field along the fiber direction is an unknown nonzero constant, $\varepsilon_0$, to be determined. The displacement field within the RVE can be considered as

$$\begin{aligned} u_1 &= u_1(x_1, x_2), \\ u_2 &= u_2(x_1, x_2), \\ u_3 &= \varepsilon_0 x_3 \end{aligned} \tag{1}$$

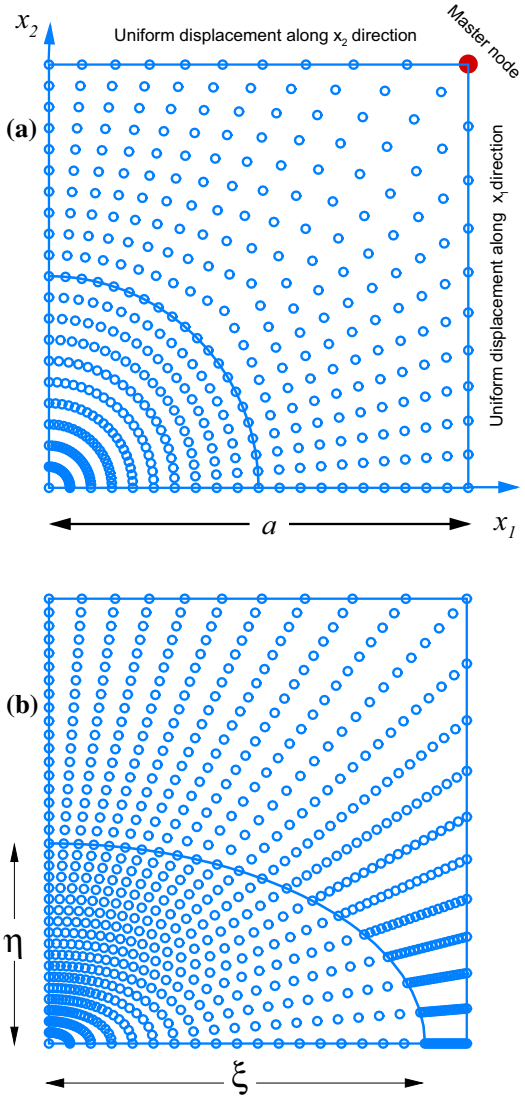


**Fig. 1** Representative volume element (RVE) for a square array of fibers with radial nodal distribution; **(a)** circular fiber; **(b)** elliptical fiber

where $u_i$ is a displacement component corresponding to the $x_i$ axis. In addition, the kinematic relations within the RVE based on the linear theory of elasticity and GPS conditions are

$$\begin{aligned} \varepsilon_{11} &= \frac{\partial u_1}{\partial x_1}; \qquad \varepsilon_{22} = \frac{\partial u_2}{\partial x_2}, \\ \varepsilon_{33} &= \frac{\partial u_3}{\partial x_3} = \varepsilon_0; \quad \varepsilon_{13} = \frac{\partial u_1}{\partial x_3} + \frac{\partial u_3}{\partial x_1} = 0, \\ \varepsilon_{12} &= \frac{\partial u_1}{\partial x_2} + \frac{\partial u_2}{\partial x_1}; \; \varepsilon_{23} = \frac{\partial u_3}{\partial x_2} + \frac{\partial u_2}{\partial x_3} = 0. \end{aligned} \tag{2}$$

As can be observed, the out of plane shear strains, $\varepsilon_{13}$ and $\varepsilon_{23}$, are zero due to the GPS conditions, which lead to zero shear stresses, $\sigma_{13} = \sigma_{23} = 0$.

## 2.2 Basic relations of piezoelectric materials

A continuum medium with domain $\Omega$ as shown in Fig. 1, which is in static mechanical and electrical equilibrium conditions, is considered. For stationary behavior of the piezoelectric material in the absence of body forces, the

weak form of the mechanical equilibrium equation [20,22] can be derived by considering the GPS conditions as

$$\int_{\Omega} \left(\delta\varepsilon^{\mathrm{T}}\sigma\right) \mathrm{d}\Omega + \int_{\Omega} \left(\delta\varepsilon_0\sigma_{\mathrm{axial}}\right) \mathrm{d}\Omega - \int_{\Gamma_t} \delta\mathbf{u}^{\mathrm{T}}\bar{\mathbf{t}}\mathrm{d}\Gamma \quad - \int_{\Omega} \delta\varepsilon_0 t_{\mathrm{axial}}\mathrm{d}\Omega = 0 \tag{3}$$

where $\varepsilon$, $\sigma$, $\mathbf{u}$ and $\bar{\mathbf{t}}$ are vectors of in-plane strains, stresses, displacements and traction loads acting upon the boundary $\Gamma_t$, which can be defined, respectively, as

$$\begin{aligned} \sigma &= \left\langle \sigma_{11}\ \sigma_{22}\ \sigma_{12} \right\rangle^{\mathrm{T}}; \quad \bar{\mathbf{u}} = \left\langle u_1\ u_2 \right\rangle^{\mathrm{T}}, \\ \varepsilon &= \left\langle \varepsilon_{11}\ \varepsilon_{22}\ \varepsilon_{12} \right\rangle^{\mathrm{T}}; \quad \bar{\mathbf{t}} = \left\langle t_1\ t_2 \right\rangle^{\mathrm{T}}, \end{aligned} \tag{4}$$

in which $\varepsilon_0$, $\sigma_{\mathrm{axial}}$ and $t_{\mathrm{axial}}$ are the constant axial strain, axial stress and traction load along the fiber direction, respectively. In this study, piezoelectric fibers within the RVE are polarized in the $x_3$ direction. Consequently, it is assumed that the electric field is confined just to the $E_3$ component, and the other two components vanish. The variational form of Maxwell's equation in the presence of electric charge upon a surface $\Omega'$ which is perpendicular to the polarization direction, i.e., $x_3$ can be derived as

$$\int_{\Omega} \delta E_3 D_3 \mathrm{d}\Omega - \int_{\Omega'} \delta E_3 q_3 \mathrm{d}\Omega = 0 \tag{5}$$

in which $E_3$, $D_3$ and $q_3$ are components of electric field, electric flux density and electric charge density vectors in the $x_3$ direction, respectively. The electric flux density is occasionally denoted as electric displacement. In addition, for the case of longitudinal polarization, in which the $x_1 - x_2$ plane would be the solution domain, $\sigma_{\mathrm{axial}} = \sigma_{33}$, $t_{\mathrm{axial}} = t_3$ and $\Omega' = \Omega$. The constitutive equations of piezoelectric materials with polarization along the $x_3$ direction which describe the coupled interaction between electrical and mechanical variables are expressed as

$$\begin{aligned} \sigma &= C\varepsilon + \widehat{\mathbf{C}}\varepsilon_0 - \widehat{\mathbf{e}}E_3, \\ \sigma_{33} &= \widehat{C}^{\mathrm{T}}\varepsilon + c_{33}\varepsilon_0 - e_{33}E_3, \\ D_3 &= \widehat{e}^{\mathrm{T}}\varepsilon + e_{33}\varepsilon_0 + \kappa_{33}E_3 \end{aligned} \tag{6}$$

where $\mathbf{C}$, $\widehat{\mathbf{C}}$ and $\widehat{\mathbf{e}}$ are defined as

$$\begin{aligned} \mathbf{C} &= \begin{pmatrix} c_{11} & c_{12} & 0 \\ c_{12} & c_{22} & 0 \\ 0 & 0 & c_{66} \end{pmatrix}; \quad \widehat{\mathbf{C}} = \left\langle c_{13}\ c_{23}\ 0 \right\rangle^{\mathrm{T}}, \\ \widehat{\mathbf{e}} &= \left\langle e_{31}\ e_{32}\ 0 \right\rangle^{\mathrm{T}}. \end{aligned} \tag{7}$$

It should be noted that in the aforementioned constitutive relations, the quantities $C_{ij}$, $e_{ij}$ and $\kappa_{ij}$ denote components of stiffness, piezoelectric and permittivity matrices, respectively.

### 2.3 Element-free Galerkin (EFG) method

The mesh-free methods have attracted considerable attention for the solution and simulation of physical problems. Several researchers employed various mesh-free methods to obtain solutions for the governing equations in the micromechanics of heterogeneous materials [23–25]. Lack of mesh structure, which eliminates the difficulty of mesh generation, can be considered as a significant feature of mesh-free methods. EFG method, which was developed by Belytschko et al. [26,27], is one of the well-known techniques in the field of mesh-free methods. Among mesh-free methods, the EFG provides high convergence rate and more accurate results in comparison with other techniques [22,26]. In addition, the derivatives of the primary-dependent variables, such as stress fields, are already very smooth, whereas in the FE method various types of post-processing, such as $L_2$ norm, are used to smooth secondary variables, e.g., stress and/or strain contour plots [27].

*2.3.1 The Moving Least-Square (MLS) approximation*

Consider an unknown field variable $u(\mathbf{x})$, e.g., displacement in an elasticity problem, defined on the domain $\Omega$, and $\mathbf{x}$ is a vector of spatial coordinates that in the case of 2D problems has two components, i.e., $\mathbf{x}^{\mathrm{T}} = \langle x \ y \rangle$. Suppose that $u^h(\mathbf{x})$ is the approximate function of $u(\mathbf{x})$ as

$$u(\mathbf{x}) \approx u^h(\mathbf{x}) = \sum_{i=1}^{m} p_i(\mathbf{x}) \cdot a_i(\mathbf{x}) = \mathbf{P}^{\mathrm{T}}(\mathbf{x}) \cdot \mathbf{a}(\mathbf{x}) \tag{8}$$

where $\mathbf{P}(\mathbf{x})$ is a vector of basis functions, which is often built from monomials. In addition, $m$ is a number of basis functions and $\mathbf{a}(\mathbf{x})$ is a vector of unknown coefficients given by

$$\mathbf{a}^{\mathrm{T}}(\mathbf{x}) = \langle a_1(x) \ a_2(x) \cdots a_m(x) \rangle. \tag{9}$$

The vector of the coefficients can be obtained by minimizing the following functional [22]:

$$J = \sum_{i=1}^{n} \widehat{w}(\mathbf{x} - \mathbf{x}_i)\left(\mathbf{P}^{\mathrm{T}}(\mathbf{x}_i)\mathbf{a}(\mathbf{x}) - u_i\right)^2 \tag{10}$$

where $n$ is a number of nodes in the neighborhood of the point $\mathbf{x}$ and $\widehat{w}(\mathbf{x}-\mathbf{x}_i)$ is a weight function, corresponding to the distance between the sampling point $\mathbf{x}$ and the nodal coordinates $\mathbf{x}_i$. In addition, $u_i$ is the nodal parameter of $u$. The optimum values of coefficients $\mathbf{a}(\mathbf{x})$ which minimize the $J$ parameter are given by the solution of

$$\frac{\partial J}{\partial a_i} = 0; \quad i = 1, \ldots, m. \tag{11}$$

This gives the following set of linear equations [22]:

$$\mathbf{A}(\mathbf{x}) \cdot \mathbf{a}(\mathbf{x}) = \mathbf{B}(\mathbf{x}) \cdot \mathbf{U}_s \tag{12}$$

where $\mathbf{U}_s$ is a vector of the nodal parameter $u_i$ within the support domain of point $\mathbf{x}$. Moreover, $\mathbf{A}(\mathbf{x})$ and $\mathbf{B}(\mathbf{x})$ are defined as

$$\begin{aligned} \mathbf{A}(\mathbf{x}) &= \sum_{i=1}^{n} \widehat{w}(\mathbf{x} - \mathbf{x}_i)\mathbf{p}(\mathbf{x}_i)\mathbf{p}^{\mathrm{T}}(\mathbf{x}_i), \\ \mathbf{B}(\mathbf{x}) &= \langle \widehat{w}(\mathbf{x}-\mathbf{x}_1)\mathbf{p}(\mathbf{x}_1) \cdots \widehat{w}(\mathbf{x}-\mathbf{x}_n)\mathbf{p}(\mathbf{x}_n) \rangle. \end{aligned} \tag{13}$$

Solving the system of Eq. (13) for the unknown vector of coefficients $\mathbf{a}(\mathbf{x})$ and substituting it into Eq. (8) yields

$$u^h(\mathbf{x}) = \Phi^{\mathrm{T}}(\mathbf{x})\mathbf{U}_s, \tag{14}$$

in which $\Phi(\mathbf{x})$ denotes a vector of MLS shape functions as

$$\Phi^{\mathrm{T}}(\mathbf{x}) = \langle \phi_1(\mathbf{x}) \cdots \phi_n(\mathbf{x}) \rangle = \mathbf{P}^{\mathrm{T}}(\mathbf{x}) \cdot \mathbf{A}^{-1}(\mathbf{x}) \cdot \mathbf{B}(\mathbf{x}). \tag{15}$$

It should be noted that the MLS shape functions satisfy global continuity within the problem domain. The order of continuity of the shape function is corresponding to the order of basis functions and order of weight functions [22]. In this study, linear basis functions and a cubic spline weight function are employed as

$$\begin{aligned} \mathbf{P}^{\mathrm{T}}(\mathbf{x}) &= \langle 1 \ x \ y \rangle, \\ w(\mathbf{x} - \mathbf{x}_i) &= \begin{cases} 2/3 - 4\bar{r}_i^2 + 4\bar{r}_i^3 & \bar{r}_i \le 0.5 \\ 4/3 - 4\bar{r}_i + 4\bar{r}_i^2 - 4/3\bar{r}_i^3 & 0.5 \le \bar{r}_i \le 1 \\ 0 & \bar{r}_i > 1 \end{cases} \end{aligned} \tag{16}$$

where $\bar{r}_i = d_i / r_w$ is a non-dimensional parameter in which $d_i = \|\mathbf{x} - \mathbf{x}_i\|_2$ and $r_w$ is known as radius of the support domain. More details about weight functions of MLS approximation can be found elsewhere [21,22].

## 2.4 Boundary conditions

### *2.4.1 Periodicity and symmetry conditions of the RVE*

In this study, the composite system is considered under normal mode electromechanical loading. In order to obtain the local and/or overall behavior of the composite from the micromechanical model, proper considerations should be taken particularly in definition of boundary conditions (BCs) on the RVE to ensure periodicity and symmetry of the model. Therefore, the left and bottom sides of the model should satisfy symmetry conditions. Moreover, to guarantee periodic BCs, the nodes on the top and right edges of the RVE should be constrained to have equal displacements along the $x_2$ and the $x_1$ axes, respectively. Consequently, the symmetric and periodic BCs yield the following set of equations [28]:

$$\begin{aligned} u_1(0, x_2) &= 0, \\ u_1(a, x_2) &= a\bar{\varepsilon}_{11}, \\ u_2(x_1, 0) &= 0, \\ u_2(x_1, a) &= a\bar{\varepsilon}_{22} \end{aligned} \tag{17}$$

where $\bar{\varepsilon}_{11}$ and $\bar{\varepsilon}_{22}$ denote the average normal strains along the $x_1$ and $x_2$ axes, respectively, and the $a$ parameter is the width of the RVE, as seen in Fig. 1. Due to a lack of the Kronecker delta function of the MLS shape functions, it is not trivial to impose essential BCs. Therefore, a number of different ideas are presented to impose essential BCs, see for example [29]. The most frequently used techniques are the Lagrange multiplier [27] and the penalty [30] approaches. Both penalty and Lagrange multiplier methods are used to enforce different essential BCs. The penalty method is used to ensure displacement continuity condition at the interface of fiber–matrix, while the Lagrange multiplier method is imposed to enforce the periodic and symmetric BCs of the RVE. For the prescribed displacement $\bar{u}$ on the boundary $\Gamma_u$, e.g., left edge of the RVE, the following expression must be added to Eq. (3):

$$\int_{\Gamma_u} \delta\lambda^{\mathrm{T}}(\mathbf{u} - \bar{\mathbf{u}})\mathrm{d}\Gamma + \int_{\Gamma_u} \delta\mathbf{u}^{\mathrm{T}}\lambda\mathrm{d}\Gamma \tag{18}$$

where $\lambda$ denotes a vector of Lagrange multipliers. In addition, the nodes on the top and right edges of the model are constrained to the specific node, which is called "master node," as shown in Fig. 1, to ensure the periodicity condition of the RVE. To this end, the following expression must be added to Eq. (3):

$$\int_{\Gamma_t} \delta\lambda^{\mathrm{T}}\,(\mathbf{u} - \mathbf{u}_k)\,\mathrm{d}\Gamma + \int_{\Gamma_t} \delta(\mathbf{u} - \mathbf{u}_k)^{\mathrm{T}}\lambda\mathrm{d}\Gamma \tag{19}$$

where the subscript $k$ indicates the master node number.

### *2.4.2 Interface condition*

The other issue in the mesh-free method is an appropriate treatment of the material discontinuity at the fiber–matrix interface. This is due to the fact that in the mesh-free method there is no mesh of elements, and therefore the interface of fiber–matrix cannot be defined based on the elements. In this study, a fully bonded fiber–matrix interface is considered. To this end, the continuity of the nodal displacements on the fiber–matrix interface must be satisfied. It should be noted that once the continuity of the displacements are satisfied, the continuity of the tractions on the interface boundary will be approximately satisfied [31],

$$\mathbf{u}^f = \mathbf{u}^m, \tag{20}$$

where $\mathbf{u}^m$ and $\mathbf{u}^f$ denote displacement parameters of the fiber and the matrix, respectively, on the interface boundary.

In this study, the penalty method was used to deal with the material discontinuity problem. A set of nodes is assigned on the interface boundary, which participate in both of the fiber and matrix domains. Consequently, the continuity of the fiber–matrix interface can be imposed by means of a penalty formulation as [32]

$$\int_{\Gamma_c} \delta\left(\mathbf{u}^f - \mathbf{u}^m\right)^{\mathrm{T}} \alpha \left(\mathbf{u}^f - \mathbf{u}^m\right) \mathrm{d}\Gamma \tag{21}$$

where $\alpha$ is the $2 \times 2$ diagonal matrix of the penalty factor. It should be noted that the success of this method is directly associated with the usage of a large number for $\alpha$. The advantages of the penalty method are that the size of the system of linear equations is constant and the possibility of the positive definiteness of the global stiffness matrix remains for large enough $\alpha$.

### 2.5 Numerical integration

Using weighted residuals approaches, one may obtain the weak form of the governing partial differential equation (PDE) of the problem. This weak form of the PDEs contains integration terms, which should be assessed numerically. The Gauss quadrature numerical integration is frequently used for the integration in the mesh-free methods. This needs quadrature points within the solution domain, which are distributed based on the roots of Legendre polynomials. Therefore, a global background cell structure is employed to perform integrations. Moreover, it should be noted that the fourth-order Gauss quadrature integration is used in this study.

### 2.6 Numerical discretization

Based on the EFG method, the weak form of equilibrium equations, i.e., Eqs. (3) and (5), is approximated by the MLS shape functions. Therefore, the approximated displacement field can be written as

$$\mathbf{u}^h(\mathbf{x}) = \begin{Bmatrix} u^h \\ v^h \end{Bmatrix} = \sum_{I=1}^{n} \begin{pmatrix} \phi_I & 0 \\ 0 & \phi_I \end{pmatrix} \begin{Bmatrix} u_I \\ v_I \end{Bmatrix} = \sum_{I=1}^{n} \tilde{\Phi}_I \mathbf{u}_I \tag{22}$$

where $\tilde{\Phi}_I(\mathbf{x})$ is the diagonal matrix of the shape function of node $I$, and $\mathbf{u}_I$ and $\mathbf{u}^h(\mathbf{x})$ are the nodal parameter of the displacement and approximate displacement at sampling point $\mathbf{x}$, respectively. Furthermore, $n$ is the number of nodes in the support of sampling point $\mathbf{x}$, which participates in the approximation scheme. The discretized form of Eq. (3) is

$$\begin{aligned} &\sum_{I=1}^{N}\sum_{J=1}^{N} \delta\mathbf{u}_I^{\mathrm{T}} \left( \int_{\Omega} \mathbf{B}_I^{\mathrm{T}} \mathbf{C} \mathbf{B}_J \mathrm{d}\Omega \right) \mathbf{u}_J + \sum_{I=1}^{N} \delta\mathbf{u}_I^{\mathrm{T}} \left( \int_{\Omega} \mathbf{B}_I^{\mathrm{T}} \widehat{\mathbf{C}} \mathrm{d}\Omega \right) \varepsilon_0 - \sum_{I=1}^{N} \delta\mathbf{u}_I^{\mathrm{T}} \left( \int_{\Omega} \mathbf{B}_I^{\mathrm{T}} \widehat{\mathbf{e}} \mathrm{d}\Omega \right) E_3 + \\ &+ \sum_{I=1}^{N} \delta\varepsilon_0 \left( \int_{\Omega} \widehat{\mathbf{C}}^{\mathrm{T}} \mathbf{B}_I \mathrm{d}\Omega \right) \mathbf{u}_I + \delta\varepsilon_0 \left( \int_{\Omega} c_{33} \mathrm{d}\Omega \right) \varepsilon_0 - \delta\varepsilon_0 \left( \int_{\Omega} e_{33} \mathrm{d}\Omega \right) E_3 - \\ &- \sum_{I=1}^{N} \delta\mathbf{u}_I^{\mathrm{T}} \left( \int_{\Gamma_t} \tilde{\Phi}_I^{\mathrm{T}} \bar{\mathbf{t}} \mathrm{d}\Gamma \right) - \delta\varepsilon_0 \int_{\Omega} t_3 \mathrm{d}\Omega = 0 \end{aligned} \tag{23}$$

where $N$ is the number of nodes in the global domain and $\mathbf{B}_I$ is defined as

$$\mathbf{B}_I = \begin{pmatrix} \phi_{I,1} & 0 \\ 0 & \phi_{I,2} \\ \phi_{I,2} & \phi_{I,1} \end{pmatrix}. \tag{24}$$

It is possible to rewrite Eq. (23) in a compact form as

$$\begin{aligned} &\delta\mathbf{U}^{\mathrm{T}} \left( \mathbf{K}\mathbf{U} + \mathbf{F_1}\varepsilon_0 - \mathbf{F_2}E_3 - \mathbf{f_t} \right) \\ &+\delta\varepsilon_0 \left( \mathbf{F}_1^{\mathrm{T}}\mathbf{U} + X_1\varepsilon_0 - X_2 E_3 - f_{\mathrm{axial}} \right) = 0 \end{aligned} \tag{25}$$

in which

$$\begin{aligned}
\mathbf{K}_{IJ} &= \int_{\Omega} \mathbf{B}_I^{\mathrm{T}} \mathbf{C} \mathbf{B}_J \mathrm{d}\Omega, \\
\mathbf{F}_{1I} &= \int_{\Omega} \mathbf{B}_I^{\mathrm{T}} \widehat{\mathbf{C}} \mathrm{d}\Omega; \quad \mathbf{F_2}_I = \int_{\Omega} \mathbf{B}_I^{\mathrm{T}} \widehat{\mathbf{e}} \mathrm{d}\Omega, \\
\mathbf{f_t}_I &= \int_{\Gamma_t} \tilde{\Phi}_I^{\mathrm{T}} \bar{\mathbf{t}} \mathrm{d}\Gamma; \quad \mathrm{f_{axial}} = \int_{\Omega} t_3 \mathrm{d}\Omega, \\
X_1 &= \int_{\Omega} c_{33} \mathrm{d}\Omega; \quad X_2 = \int_{\Omega} e_{33} \mathrm{d}\Omega.
\end{aligned} \tag{26}$$

The next step is related to the enforcement of the essential BCs. As mentioned before, the Lagrange multiplier method is an appropriate way to enforce essential BCs. To this end, a new type of shape functions, which is used in conventional FE method, is considered to discretize the Lagrange multipliers. Linear interpolation is used to approximate the Lagrange multipliers between two nodes on the essential BCs. The Lagrange linear shape functions for two adjacent nodes are defined as

$$N_0(s) = \frac{s - s_1}{s_0 - s_1}, \quad N_1(s) = \frac{s - s_0}{s_1 - s_0} \tag{27}$$

where $s$ is the parameter of arc-length. For the left and bottom edges of the RVE, the final discretized form of expression (18) can be written as

$$\begin{aligned}
&\sum_{I=1}^{N_\lambda^1} \sum_{J=1}^{N} \delta\lambda_I^{\mathrm{T}} \left( \int_{\Gamma_u} \mathbf{N}_I^{\mathrm{T}} \tilde{\Phi}_J \mathrm{d}\Gamma \right) \mathbf{u}_J - \sum_{I=1}^{N_\lambda^1} \delta\lambda_I^{\mathrm{T}} \left( \int_{\Gamma_u} \mathbf{N}_I^{\mathrm{T}} \bar{\mathbf{u}} \mathrm{d}\Gamma \right) \\
&+ \sum_{I=1}^{N_\lambda^1} \sum_{J=1}^{N} \delta\mathbf{u}_J^{\mathrm{T}} \left( \int_{\Gamma_u} \tilde{\Phi}_J^{\mathrm{T}} \mathbf{N}_I \mathrm{d}\Gamma \right) \lambda_I
\end{aligned} \tag{28}$$

where $\mathbf{N}_I$ is the diagonal matrix of Lagrange shape functions and $N_\lambda^1$ is the number of nodes on the left and/or bottom edges of the RVE. In the compact form, expression (28) can be written as

$$\delta \Lambda_1^{\mathrm{T}} (\mathbf{G}\mathbf{U} - \mathbf{P}) + \delta \mathbf{U}^{\mathrm{T}} \mathbf{G}^{\mathrm{T}} \Lambda_1 \tag{29}$$

where $\Lambda_1$ is a vector of Lagrange multipliers associated with each node on the prescribed boundary and $\mathbf{G}$ and $\mathbf{P}$ matrices are

$$\begin{aligned}
G_{IJ} &= \int_{\Gamma_u} \mathbf{N}_I^{\mathrm{T}} \tilde{\Phi}_J \mathrm{d}\Gamma, \\
P_I &= \int_{\Gamma_u} \mathbf{N}_I^{\mathrm{T}} \bar{\mathbf{u}} \mathrm{d}\Gamma.
\end{aligned} \tag{30}$$

Moreover, the final discretized form of expression (19) can be written as

$$\begin{aligned}
&\sum_{I=1}^{N_\lambda^2} \sum_{J=1}^{N} \delta\lambda_I^{\mathrm{T}} \left( \int_{\Gamma_t} \mathbf{N}_I^{\mathrm{T}} \tilde{\Phi}_J \mathrm{d}\Gamma \right) \mathbf{u}_J - \sum_{I=1}^{N_\lambda^2} \sum_{J=1}^{N} \delta\lambda_I^{\mathrm{T}} \left( \int_{\Gamma_t} \mathbf{N}_I^{\mathrm{T}} \mathrm{d}\Gamma \right) \delta_{JK} \mathbf{u}_J \\
&+ \sum_{I=1}^{N_\lambda^2} \sum_{J=1}^{N} \delta\mathbf{u}_J^{\mathrm{T}} \left( \int_{\Gamma_t} \tilde{\Phi}_J^{\mathrm{T}} \mathbf{N}_I \mathrm{d}\Gamma \right) \lambda_I - \sum_{I=1}^{N_\lambda^2} \sum_{J=1}^{N} \delta\mathbf{u}_J^{\mathrm{T}} \left( \int_{\Gamma_t} \mathbf{N}_I \mathrm{d}\Gamma \right) \delta_{JK} \lambda_I
\end{aligned} \tag{31}$$

where $N_{\lambda}^{2}$ is the number of nodes on the right and/or top edges of the RVE. Furthermore, $\delta$ indicates the Kronecker delta function. In a compact form, expression (31) can be expressed as

$$\delta \Lambda_2^{\mathrm{T}} \mathbf{G}^{*} \mathbf{U} + \delta \mathbf{U}^{\mathrm{T}} \mathbf{G}^{*\mathrm{T}} \Lambda_2 \tag{32}$$

where $\Lambda_2$ is a vector of Lagrange multipliers corresponding to each node on the right and/or top edges of the RVE. Moreover, $\mathbf{G}^{*} = \mathbf{G} - \mathbf{H}$, while $\mathbf{H}$ is

$$H_{IJ} = \delta_{JK} \int_{\Gamma_t} \mathbf{N}_I^{\mathrm{T}} \mathrm{d}\Gamma \tag{33}$$

in which, as previously mentioned, $K$ denotes the master node number. The discretized form of Eq. (21), which is related to the fiber–matrix interface boundary, takes the following compact form:

$$\delta \mathbf{U}^{\mathrm{T}} \mathbf{K}^{\alpha} \mathbf{U} \tag{34}$$

where

$$K_{IJ}^{\alpha} = \int_{\Gamma_c} \left[ \tilde{\Phi}_I^m - \tilde{\Phi}_I^f \right]^{\mathrm{T}} \alpha \left[ \tilde{\Phi}_J^m - \tilde{\Phi}_J^f \right] \mathrm{d}\Gamma; \quad I, J = 1, \ldots N \tag{35}$$

in which $\tilde{\Phi}_I^f$ and $\tilde{\Phi}_I^m$ are the diagonal matrices of the shape functions of node $I$ for the fiber and matrix domains, respectively. Consequently, the final form of the mechanical equilibrium equation can be recovered using Eqs. (25), (29), (32) and (34) as

$$\begin{aligned} &\delta \mathbf{U}^{\mathrm{T}} \left\{ \left( \mathbf{K} + \mathbf{K}^{\alpha} \right) \mathbf{U} + \mathbf{F_1} \varepsilon_0 + \mathbf{G}^{\mathrm{T}} \Lambda_1 \quad + \mathbf{G}^{*\mathrm{T}} \Lambda_2 - \mathbf{F_2} E_3 - \mathbf{f_t} \right\} + \delta \Lambda_1^{\mathrm{T}} \left( \mathbf{G}\mathbf{U} - \mathbf{P} \right) + \delta \Lambda_2^{\mathrm{T}} \left( \mathbf{G}^{*} \mathbf{U} \right) \\ &+ \delta \varepsilon_0 \left( \mathbf{F}_1^{\mathrm{T}} \mathbf{U} + X_1 \varepsilon_0 - X_2 E_3 - f_{\mathrm{axial}} \right) = 0. \end{aligned} \tag{36}$$

The discretized form of the electrical equilibrium Eq. (5) is

$$\begin{aligned} &\sum_{I=1}^{N} \delta E_3 \left( \int_{\Omega} \widehat{\mathbf{e}}^{\mathrm{T}} \mathbf{B}_I \mathrm{d}\Omega \right) \mathbf{u}_I + \delta E_3 \left( \int_{\Omega} e_{33} \mathrm{d}\Omega \right) \varepsilon_0 \\ &+ \delta E_3 \left( \int_{\Omega} \kappa_{33} \mathrm{d}\Omega \right) E_3 + \delta E_3 \left( \int_{\Omega'} q_3 \mathrm{d}\Omega \right) = 0. \end{aligned} \tag{37}$$

Equation (37) can be rewritten in a compact form as

$$\delta E_3 \left( \mathbf{F}_2^{\mathrm{T}} \mathbf{U} + X_2 \varepsilon_0 + X_3 E_3 + Q_3 \right) = 0 \tag{38}$$

in which

$$X_3 = \int_{\Omega} \kappa_{33} \mathrm{d}\Omega; \quad \mathrm{Q}_3 = \int_{\Omega'} q_3 \mathrm{d}\Omega. \tag{39}$$

Since $\delta \mathbf{U}$, $\delta \varepsilon_0$, and $\delta E_3$ are arbitrary, the expressions within the parentheses must be zero to ensure satisfaction of Eqs. (36) and (38). Therefore, the governing equations in a discretized form appear as the following linear system of equations:

$$\begin{cases} \left( \mathbf{K} + \mathbf{K}^{\alpha} \right) \mathbf{U} + \mathbf{F_1} \varepsilon_0 - \mathbf{F_2} E_3 + \mathbf{G}^{\mathrm{T}} \Lambda_1 + \mathbf{G}^{*\mathrm{T}} \Lambda_2 - \mathbf{f_t} = 0 \\ \mathbf{F}_1^{\mathrm{T}} \mathbf{U} + X_1 \varepsilon_0 - X_2 E_3 - f_{\mathrm{axial}} = 0 \\ \mathbf{F}_2^{\mathrm{T}} \mathbf{U} + X_2 \varepsilon_0 + X_3 E_3 + Q_3 = 0 \\ \mathbf{G}\mathbf{U} - \mathbf{P} = 0 \\ \mathbf{G}^{*} \mathbf{U} = 0 \end{cases} \tag{40}$$

or in a matrix form as

$$\begin{pmatrix} (\mathbf{K}+\mathbf{K}^{\alpha}) & \{\mathbf{F}_1\} & \{\mathbf{F}_2\} & (\mathbf{G}^{\mathrm{T}}) & \left(\mathbf{G}^{*\mathrm{T}}\right) \\ \langle \mathbf{F}_1^{\mathrm{T}} \rangle & X_1 & X_2 & 0 & 0 \\ \langle \mathbf{F}_2^{\mathrm{T}} \rangle & X_2 & -X_3 & 0 & 0 \\ (\mathbf{G}) & 0 & 0 & 0 & 0 \\ (\mathbf{G}^{*}) & 0 & 0 & 0 & 0 \end{pmatrix} \begin{Bmatrix} \{\mathbf{U}\} \\ \varepsilon_0 \\ -E_3 \\ \{\Lambda_1\} \\ \{\Lambda_2\} \end{Bmatrix} = \begin{Bmatrix} \{\mathbf{f_t}\} \\ f_{\text{axial}} \\ -Q_3 \\ \{\mathbf{P}\} \\ 0 \end{Bmatrix}. \tag{41}$$

In order to solve the system of linear equations (41), the Gauss elimination technique is employed to obtain results of nodal parameters of the displacements, the axial strain and electric field along the polarization direction. It should be noted that the displacements at any point including field nodes in the domain can be obtained from (14).

## 3 Results and discussion

### 3.1 Parallel processing aspects of the EFG method

As previously mentioned in Sect. 2.3, the EFG method provides several major advantages such as lack of mesh structure, high convergence rate and higher-order continuous shape functions. It should, however, be noted that mesh-free methods in general suffer from various disadvantages. While considerable attempts have been made recently to improve mesh-free methods, currently available methods are still computationally less efficient in comparison with the well-established conventional discretization techniques such as FEM. To this end, one may refer to the following points as main reasons which may cause additional computational costs in the EFG method:

1. The determination of the influence domain for each Gauss point,
2. The relative complexity of the EFG shape functions
3. Additional attempts to enforce essential boundary conditions using Lagrange multiplier method

Due to the above reasons, one may conclude that the EFG procedure would be time-consuming when compared to the FEM. However, parallelization can be considered as a simple way to speed up the EFG technique. The result of parallelization for the presented EFG code is examined using OpenMP application programming interface. It should be mentioned that the OpenMP has been widely used for parallelization as it needs just a few changes in a sequential code and therefore requires an easy procedure for implementation. In order to capture the relative benefit of a numerical procedure, the speedup parameter is normally used which is commonly defined as the time ratio of the serial algorithm to the parallel algorithm for a specific computer program. Figure 2 depicts the variation of the speedup parameter of the present EFG method versus the number of processors. The figure indicates that for ten processors the maximum speedup reaches 9.04 for a moderate and sufficient number of nodes. This implies that the presented EFG method exhibits excellent parallelization capability. Discrepancies between the ideal graph, which is raised from Amdahls law [33], and the presented results are due to the fact that any part of a program which cannot be parallelized can be considered as a bottleneck which limits the speedup.

### 3.2 The overall electro-elastic behavior of PFRCs

Using the present EFG micromechanical model, electro-elastic coefficients related to normal mode sensing and actuation are predicted for both axial and transverse polarization. In order to study the effects of fiber shape on the electro-elastic behavior of PFRCs, two different types of fiber cross sections including circular and elliptical fibers are considered in both axial and transverse polarization cases, see Figs. 1 and 3. To facilitate comparison of effective coefficients of PFRCs with corresponding coefficients of a pure piezoelectric material, it is preferred to use normalized electro-elastic coefficients as

$$e_{ij}^{*} = \frac{e_{ij}}{e_{ij}^{\mathrm{P}}}; \quad \mathrm{Y}_i^{*} = \frac{Y_i}{Y_i^{\mathrm{P}}}; \quad \kappa_{33}^{*} = \frac{\kappa_{33}}{\kappa_0} \tag{42}$$

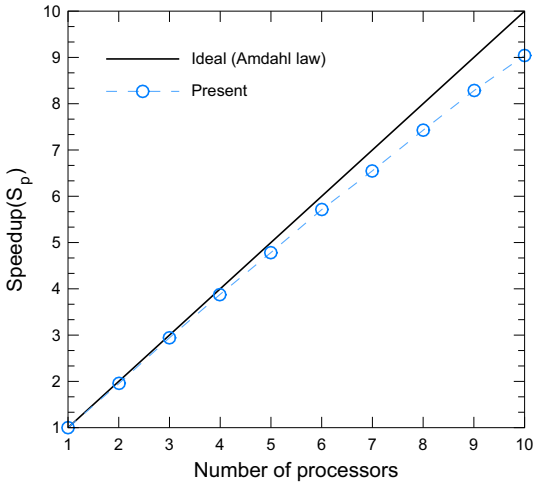


**Fig. 2** Variation of speedup (Sp) of the present EFG method versus the number of processors

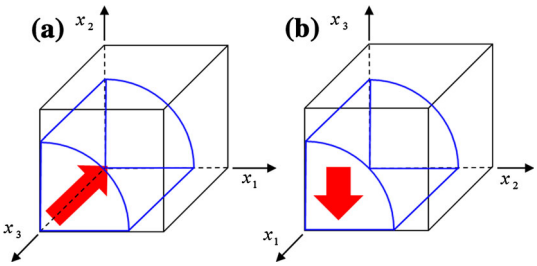


**Fig. 3** Coordinate system with electric field direction depicted by arrows; **(a)** axial polarization; **(b)** transverse polarization

**Table 1** Electro-elastic coefficients of matrix and fiber materials [6,7]

| Material | Elastic constants(GPa) | | | | | | Dielectric constant $(F/m)$ | Piezoelectric constants $(C/m^2)$ | |
|---|---|---|---|---|---|---|---|---|---|
| | $C_{11}=C_{22}$ | $C_{12}$ | $C_{13}=C_{23}$ | $C_{33}$ | $C_{44}=C_{55}$ | $C_{66}$ | $\kappa_{33}$ | $e_{31}=e_{32}$ | $e_{33}$ |
| PZT-7A | 148 | 76.2 | 74.2 | 131 | 25.4 | 35.9 | $2.07\times10^{-9}$ | –2.1 | 9.5 |
| PZT-5H | 151 | 98 | 96 | 124 | 23 | 23.3 | $13.27\times10^{-9}$ | –5.1 | 27 |
| Epoxy | 3.86 | 2.57 | 2.57 | 3.86 | 0.64 | 0.64 | $0.079\times10^{-9}$ | 0 | 0 |
| Polyimide | 8.1 | 5.4 | 5.4 | 8.1 | 1.4 | 1.6 | $0.0247\times10^{-9}$ | 0 | 0 |

where $Y_i$ is an elastic modulus of composite corresponding to the $x_i$ direction and $\kappa_0$ is defined as permittivity of free space, which is equal to $8.85\times10^{-12}{}^{F}/_{m}$ [34]. Moreover, superscript P denotes a pure piezoelectric material.

### *3.2.1 Longitudinal polarization*

The first case study is related to a unidirectional composite in which fibers are poled in the direction parallel to the fiber axis, as shown in Fig. 3a. It is also assumed that the electric field is applied along the fibers direction, which has a constant and unique value in both matrix and fiber phases. Details of constituent properties of PFRC at room temperature are given in Table 1. In order to verify the present model, the electro-elastic behavior of PZT-7A/polyimide composite with circular fibers for various fiber volume fractions is compared with those obtained by other micromechanical models [7]. Both elastic and electrical constants obtained by various models including Mori-Tanaka, self-consistent and proposed by Odegard [7] together with presented EFG predictions are given in Table 2. Close agreement between the predictions of different micromechanical models can be concluded from this table. The normalized dielectric constant $\kappa_{33}^{*}$ in longitudinal polarization of PFRCs for circular and elliptical fiber shapes is shown in Fig. 4. A linear behavior is seen for this dielectric constant with respect to the fiber volume fraction. It should be noted that due to geometrical restrictions in a square array

**Table 2** Comparison of the predicted non-dimensional electro-elastic coefficients of PZT-7A/Polyimide PFRC between the present EFG method and other micromechanics models [7]

| Fiber volume fraction | Method | Normalized elastic constants | | Normalized electric constants | | |
|---|---|---|---|---|---|---|
| | | $Y_1^* = Y_2^*$ | $Y_3^*$ | $\kappa_{33}^*$ | $e_{31}^* = e_{32}^*$ | $e_{33}^*$ |
| 0.1 | Mori-Tanaka | 0.055922 | 0.142515 | 26.4 | 0.01 | 0.113906 |
| | Self-consistent | 0.055922 | 0.142515 | 26.4 | 0.006571 | 0.113906 |
| | Proposed-Odegard | 0.052658 | 0.140805 | 26.4 | 0.01 | 0.112632 |
| | **Present** | 0.052658 | 0.141660 | 26.4 | 0.008429 | 0.112632 |
| 0.4 | Mori-Tanaka | 0.087391 | 0.427422 | 97.18 | 0.039429 | 0.451634 |
| | Self-consistent | 0.116521 | 0.427422 | 97.18 | 0.048571 | 0.448975 |
| | Proposed-Odegard | 0.104199 | 0.428643 | 97.18 | 0.052381 | 0.449474 |
| | **Present** | 0.109802 | 0.428643 | 98.31 | 0.046952 | 0.449474 |
| 0.6 | Mori-Tanaka | 0.138932 | 0.619029 | 144.4 | 0.099524 | 0.672355 |
| | Self-consistent | 0.256569 | 0.619029 | 144.2 | 0.176190 | 0.659368 |
| | Proposed-Odegard | 0.182617 | 0.615731 | 144.2 | 0.099524 | 0.670526 |
| | **Present** | 0.209514 | 0.619029 | 146.7 | 0.103333 | 0.670526 |

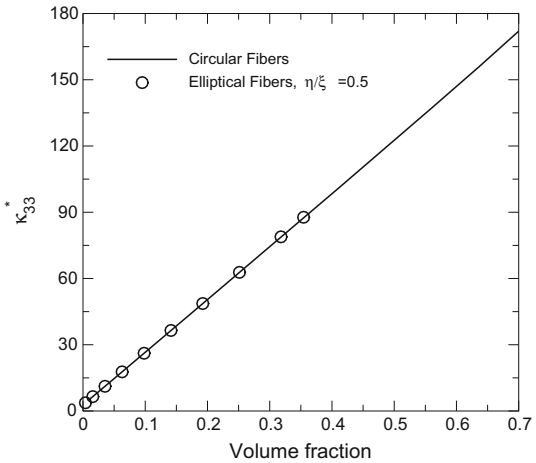


**Fig. 4** Variation of normalized dielectric coefficient $\kappa_{33}^*$ in axial polarization versus fiber volume fraction of PZT-7A/Polyimide PFRC

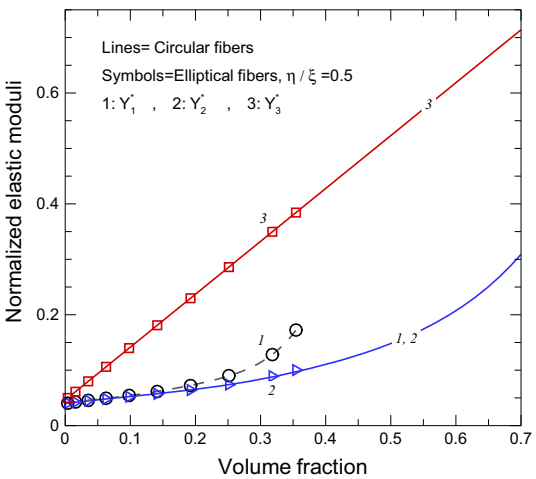


**Fig. 5** Variation of normalized elastic moduli in axial polarization versus fiber volume fraction of PZT-7A/Polyimide PFRC

packing, the volume fraction of circular and elliptical fibers with aspect ratio $(\eta/\xi)$ of 0.5 could be reached approximately up to 0.7 and 0.35, respectively. The normalized Young's moduli and piezoelectric constants are shown in Figs. 5 and 6, respectively. A linear behavior is also observed from the results of the present model

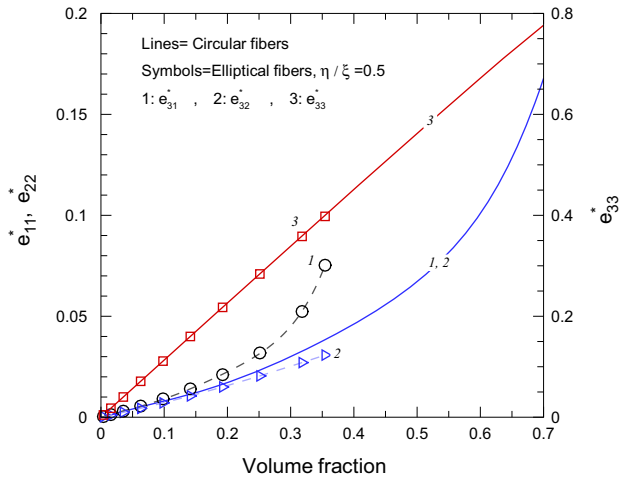


**Fig. 6** Variation of normalized piezoelectric coefficients in axial polarization versus fiber volume fraction of PZT-7A/Polyimide PFRC

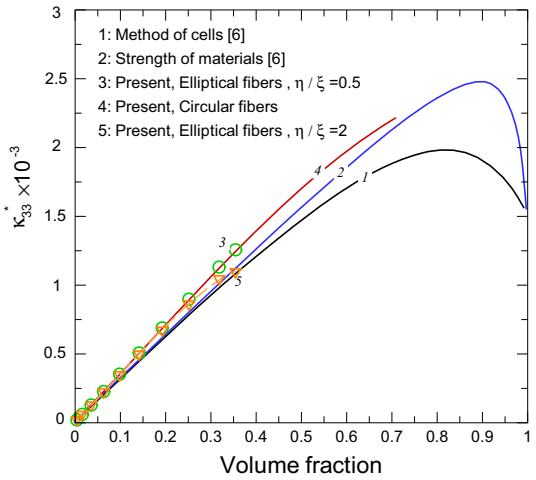


**Fig. 7** Variation of normalized dielectric coefficient $\kappa_{33}^*$ in transverse polarization versus fiber volume fraction of PZT-5H/Epoxy PFRC

for the normalized longitudinal Young's modulus $Y_3^*$ and piezoelectric constant $e_{33}^*$. Furthermore, Figs. 4, 5 and 6 also imply that the longitudinal electromechanical constants, i.e., $\kappa_{33}$, $e_{33}$ and $Y_3$, are insensitive to the fiber shape. In addition, the normalized transverse elastic moduli, i.e., $Y_1^*$ and $Y_2^*$, and normalized shear piezoelectric coefficients, i.e., $e_{31}^*$ and $e_{32}^*$, which are, respectively, shown in Figs. 5 and 6, show nonlinear behavior with respect to the fiber volume fraction. In addition, it is clear that the normalized transverse elastic modulus $Y_1^*$ and shear piezoelectric constant $e_{31}^*$ are significantly sensitive to the fiber shape. As can be seen in Figs. 5 and 6, for a volume fraction of 35 %, maximum differences between predicted values $Y_1^*$ and $e_{31}^*$ for circular and elliptical fibers are 78.9 and 50 %, respectively.

### *3.2.2 Transverse polarization*

In this case, the fibers are polarized across their thickness, as shown in Fig. 3b. Moreover, it is assumed that the electric field within both fiber and matrix phases are uniform and equal to the applied electrical field. To ensure that the direction of polarization remains unchanged in the $x_3$ direction, suitable coordinate systems for both transverse and longitudinal polarization are chosen, as shown in Fig. 3. Therefore, for the case of transverse polarization, the $x_2 - x_3$ would be the plane of symmetry and the two-dimensional solution domain. Furthermore, electromechanical constitutive relations 6 and 7 together with in-plane vectors, i.e., $\varepsilon$, $\sigma$, $\mathbf{u}$ and $\bar{\mathbf{t}}$ must be modified for the case of transverse polarization. For comparison, a PFRC consisting of PZT-5H circular fibers embedded in the epoxy matrix was considered with the electro-elastic properties presented in

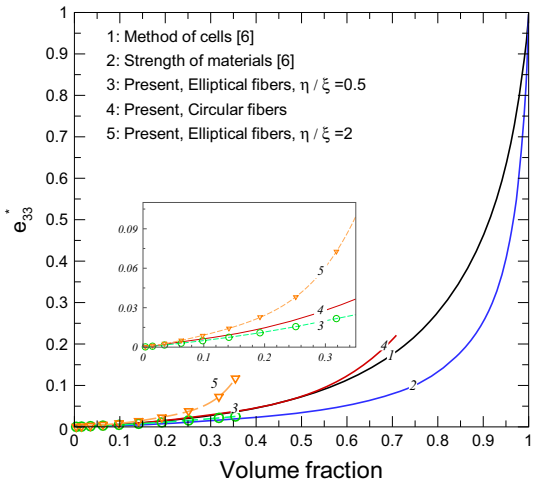


**Fig. 8** Variation of $e_{33}^{*}$ in transverse polarization versus fiber volume fraction of PZT-5H/Epoxy PFRC

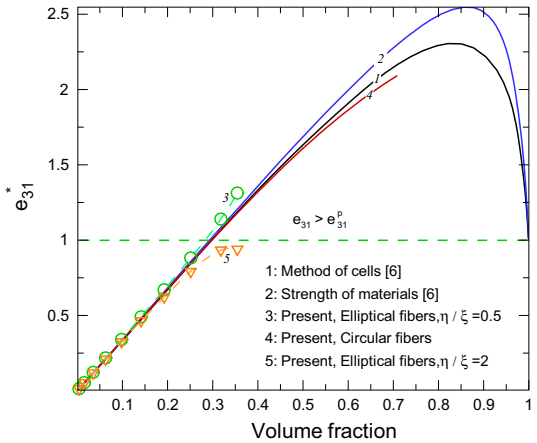


**Fig. 9** Variation of $e_{31}^{*}$ in transverse polarization versus fiber volume fraction of PZT-5H/Epoxy PFRC

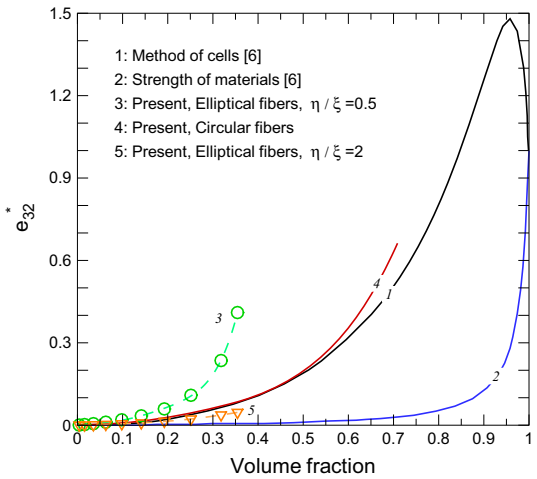


**Fig. 10** Variation of $e_{32}^{*}$ in transverse polarization versus fiber volume fraction of PZT-5H/Epoxy PFRC

Table 1. Figures 7, 8, 9 and 10 show overall electrical properties of the PZT-5H/epoxy composite system versus fiber volume fraction in transverse polarization. Included in the figures are also predictions obtained by the method of cells (MOC) and strength of materials (SM) [6], which show close agreement with results

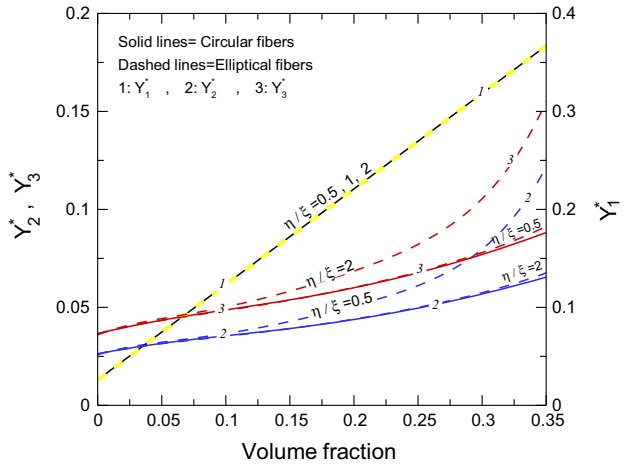


**Fig. 11** Variation of normalized elastic moduli in transverse polarization versus fiber volume fraction of PZT-5H/Epoxy PFRC

of the present EFG model. It should, however, be noted that numerical methods such as EFG provide realistic models. For instance, in analytical methods, the stress field is assumed to be uniform in both fiber and matrix phases, and the fiber shape is mostly considered to be rectangular. Predictions of the normalized dielectric constant $\kappa_{33}^*$ for elliptical fibers with three different aspect ratios, i.e., $\eta/\xi = 0.5$, 1 and 2 are shown in Fig. 7. Results reveal that in low volume fractions the predicted values of $\kappa_{33}^*$ are independent of the fiber shape, whereas slight discrepancy can be observed in the case of $\eta/\xi = 2$ at higher volume fractions. Variations of normalized effective piezoelectric coefficients with respect to the fiber volume fraction are depicted in Figs. 8, 9 and 10. It can be seen that the present EFG model and the MOC [6] are very close, while discrepancies are found between the present results and those obtained by SM [6] approach. This may be attributed to the fact that in the MOC the solution domain is subdivided into several rectangular parallelepiped sub-cells. Figure 8 depicts the nonlinear behavior of normalized piezoelectric coefficient $e_{33}^*$ with respect to the fiber volume fraction. Results reveal that increasing aspect ratio of the fiber geometry leads to an enhancement of $e_{33}^*$. The normalized effective piezoelectric coefficient $e_{31}^*$ is shown in Fig. 9. It is interesting to conclude from Fig. 9 that in PFRCs with transverse polarization and fiber volume fractions larger than about 30 % the normalized effective piezoelectric coefficient $e_{31}^*$ passes unity. This implies that the effective piezoelectric coefficient $e_{31}$ of PFRCs increases in comparison with the same coefficient for pure piezoelectric material. It should be noted that the effective coefficient $e_{31}$ in transverse polarization evaluates the amount of induced axial normal stress in PFRC due to the applied electric field. As a result, one may enhance controllability of the actuators by using PFRCs with transverse polarization. Figure 9 also shows effects of fiber shape on the performance of the normalized piezoelectric coefficient $e_{31}^*$. As may be appreciated from this figure, $e_{31}^*$ is decreased by increasing the aspect ratio of fiber geometry. Prediction of the present model about the normalized piezoelectric coefficient $e_{32}^*$ is exhibited in Fig. 10. A strong dependency of $e_{32}^*$ to the fiber shape can be observed as $e_{32}^*$ for fibers with $\eta/\xi = 0.5$ is 4.5 times that of circular fibers at 35 % volume fraction. Furthermore, similar to $e_{31}^*$, for a constant fiber volume fraction, increasing aspect ratio of the elliptical fibers significantly reduces $e_{32}^*$. Figure 11 shows the normalized Young's moduli of PFRC corresponding to various coordinate axes for three different aspect ratios of fiber geometry. The figure implies that the Young's modulus of PFRC related to the direction of orientation of the elliptical fiber major axis significantly increases in comparison with circular fibers. For instance, the normalized elastic modulus, $Y_2^*$, shows a dependency to the fiber shape; as in 35 % volume fraction, $Y_2^*$ of PFRC with elliptical fibers ($\eta/\xi = 0.5$) is 1.82 times that of PFRC with circular fibers. Moreover, it is seen that the normalized longitudinal elastic modulus, $Y_1^*$, demonstrates a linear behavior with respect to the volume fraction, while it is independent from fiber shape. Consequently, it is noteworthy that elliptical fibers can provide better electrical sensitivity in a specific direction than circular fibers for both polarization directions.

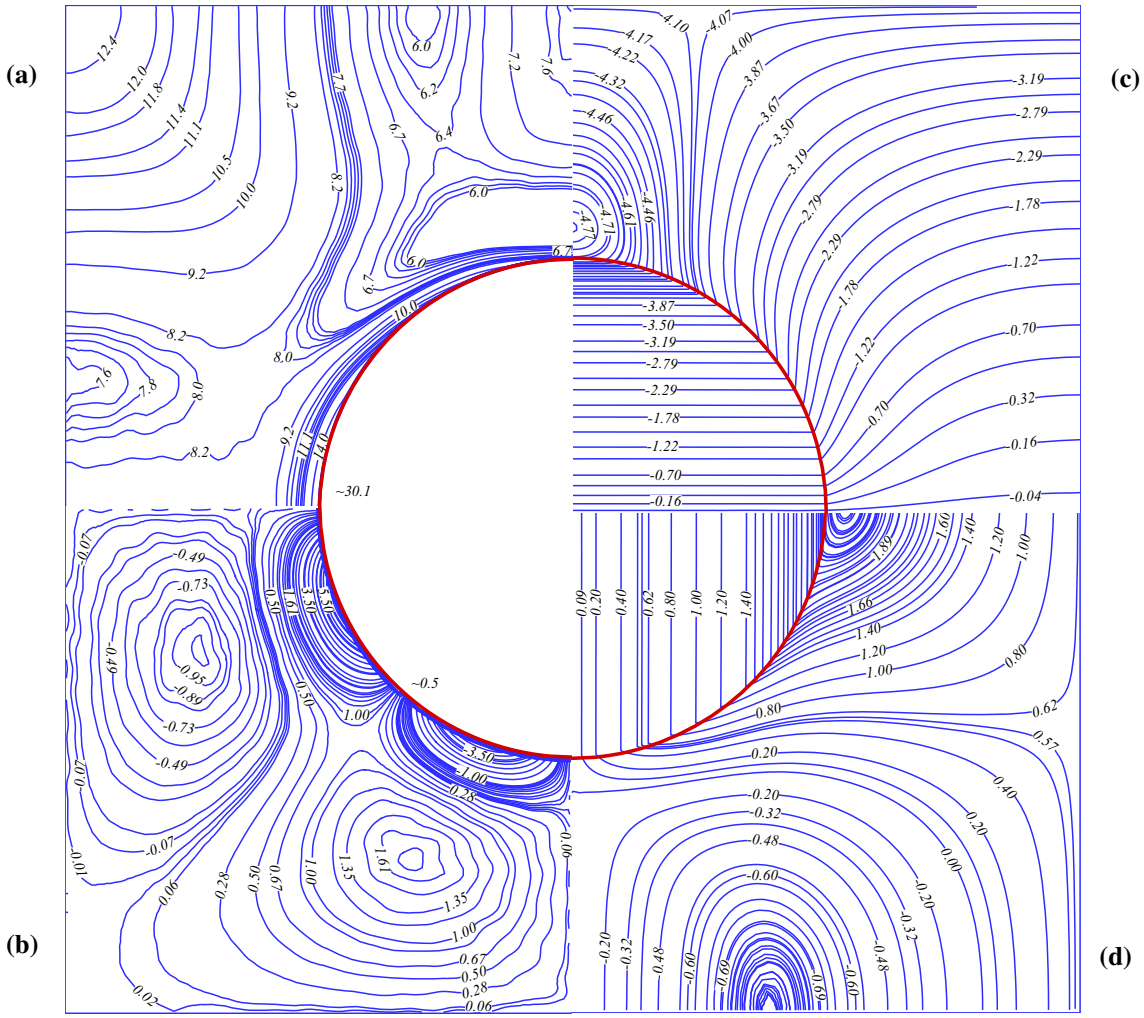


**Fig. 12** Distribution of the local fields within the RVE subjected to electric charge density $q_3 = 0.1(\text{colon}/\text{m}^2)$ on the top edge of the RVE in transverse polarization case: **(a)** von Mises stress (MPa); **(b)** shear stress (MPa); **(c)** displacement along the vertical axis (mm); **(d)** displacement along the horizontal axis (mm)

### 3.3 Local behavior of PFRCs in transverse polarization

Analytical models normally employ simplified assumptions, which can affect the physics of the problems, while they usually provide reasonably accurate predictions for axial overall properties. Moreover, in the micromechanics of composite systems, most of the analytical models are not able to present non-uniform stress and strain fields within the RVE. In the numerical methods, however, one of the interesting features is characterization of the local behavior of materials. Figure 12 shows the distribution of the local fields within the RVE subjected to electric charge density $q_3 = 0.1(\text{colon}/\text{m}^2)$ on the top edge of the standard RVE as shown in Fig. 1, in transverse polarization. Figure 12a shows the von Mises stress distribution within the RVE. It is seen that the maximum von Mises stress occurs on the horizontal axis near the fiber–matrix interface within the fiber domain. The shear stress contour plot is demonstrated in Fig. 12b. As can be seen, the shear stress tends toward zero in the vicinity of the RVE boundaries, which consequently implies that the edges of the RVE remain straight. Moreover, it may be recognized from Fig. 12a, b that the derivatives of the primary-dependent variables, which are obtained by the present EFG method, are already smooth without any post-processing. Figure 12c, d shows contour plots of displacement components along the vertical and the horizontal axes, respectively. As expected, implemented symmetric and periodic BCs and also continuity of the displacements at the fiber–matrix interface can be easily concluded.

## 4 Concluding remarks

(i) A two-dimensional generalized plane strain (GPS) micromechanical model is presented for the analysis of PFRCs subjected to the combined electrical and mechanical loading in normal mode sensing and actuation conditions.
(ii) From the numerical point of view, the EFG method provides a smooth contour plot of the derivatives of the primary-dependent variables, e.g., stress fields, without using any post-processing, such as $L_2$ norm. In addition, it is shown that the presented EFG method illustrates excellent parallelization capability. Using the parallelization tool, one may extremely reduce the computational time.
(iii) Characterizing local effects is a clear advantage of numerical methods such as EFG in comparison with analytical models. It is shown that the present mesh-free method associated with the GPS assumption provides accurate predictions. The predicted effective electro-elastic properties and those obtained by analytical methods for PFRCs indicate good agreement.
(iv) In order to study the effect of polarization direction in PFRCs, both axial and transverse polarizations are examined. It is found that beyond a critical fiber volume fraction the effective piezoelectric coefficient $e_{31}$ in PFRCs with transverse polarization considerably increases in comparison with the same coefficient for a pure piezoelectric material. Consequently, one may enhance controllability of the actuators by using PFRCs with transverse polarization.
(v) In the longitudinal polarization, the axial electro-elastic coefficients demonstrate linear behavior and insensitivity to the fiber shape. For transverse elastic moduli and shear piezoelectric coefficients, however, dependency to the fiber shapes can be seen. Results reveal that for a volume fraction of 35 % maximum differences between predicted values $Y_1^*$ and $e_{31}^*$ for circular and elliptical fibers are 78.9 and 50 %, respectively.
(vi) In the transverse polarization, results disclose that increasing aspect ratio of elliptical fiber geometry increases $e_{33}^*$, while this causes that $e_{31}^*$ and $e_{32}^*$ decrease. Furthermore, the results exhibit a strong dependency of $e_{32}^*$ to the fiber shape as $e_{32}^*$ for fibers with $\eta/\xi = 0.5$ is 4.5 times that of circular fibers at 35 % volume fraction.
(vii) As expected, results imply that the elastic modulus of PFRCs, related to the direction of orientation of the elliptical fiber major axis, significantly increases in comparison with circular fibers in both polarization directions.

## References


1. Safari, A.: Development of piezoelectric composites for transducers. J. Phys. III **4**, 1129–1149 (1994)
2. Jayendiran, R., Arockiarajan, A.: Non-linear electromechanical response of 1–3 type piezocomposites. Int. J. Solids Struct. **50**, 2259–2270 (2013)
3. Li, L., Zhang, S., Xu, Z., Wen, F., Geng, X., Lee, H.J., Shrout, T.R.: 1–3 piezoelectric composites for high-temperature transducer applications. J. Phys. D: Appl. Phys. **46**, 165306 (2013)
4. Bravo-Castillero, J., Guinovart-Dıaz, R., Sabina, F.J., Rodrıguez-Ramos, R.: Closed-form expressions for the effective coefficients of a fiber-reinforced composite with transversely isotropic constituents–II. piezoelectric and square symmetry. Mech. Mater. **33**, 237–248 (2001)
5. Tan, P., Tong, L.: Modeling for the electro-magneto-thermo-elastic properties of piezoelectric-magnetic fiber reinforced composites. Compos. A: Appl. Sci. Manuf. **33**, 631–645 (2002)
6. Mallik, N., Ray, M.C.: Effective coefficients of piezoelectric fiber-reinforced composites. AIAA J. **41**, 704–710 (2003)
7. Odegard, G.M.: Constitutive modeling of piezoelectric polymer composites. Acta Mater. **52**, 5315–5330 (2004)
8. Berger, H., Kari, S., Gabbert, U., Rodriguez-Ramos, R., Guinovart, R., Otero, J.A., Bravo-Castillero, J.: An analytical and numerical approach for calculating effective material coefficients of piezoelectric fiber composites. Int. J. Solids Struct. **42**, 5692–5714 (2005)
9. Ray, M.C.: Micromechanics of piezoelectric composites with improved effective piezoelectric constant. Int. J. Mech. Mater. Des. **3**, 361–371 (2006)
10. Della, C.N., Shu, D.: On the performance of 1–3 piezoelectric composites with a passive and active matrix. Sens. Actuators A: Phys. **140**, 200–206 (2007)
11. Kar-Gupta, R., Venkatesh, T.A.: Electromechanical response of 1–3 piezoelectric composites: an analytical model. Acta Mater. **55**, 1093–1108 (2007)
12. Kumar, A., Chakraborty, D.: Effective properties of thermo-electro-mechanically coupled piezoelectric fiber reinforced composites. Mater. Des. **30**, 1216–1222 (2009)
13. Sakthivel, M., Arockiarajan, A.: An analytical model for predicting thermo-electro-mechanical response of 1–3 piezoelectric composites. Comput. Mater. Sci. **48**, 759–767 (2010)
14. Guinovart-Díaz, R., Yan, P., Rodríguez-Ramos, R., López-Realpozo, J.C., Jiang, C.P., Bravo-Castillero, J., Sabina, F.J.: Effective properties of piezoelectric composites with parallelogram periodic cells. Int. J. Eng. Sci. **53**, 58–66 (2012)

15. López-López, E., Sabina, F.J., Guinovart-Díaz, R., Bravo-Castillero, J., Rodríguez-Ramos, R.: Effective permittivity of a fiber-reinforced composite with transversely isotropic constituents. J. Electrost. **71**, 791–800 (2013)
16. Lin, C.-H., Muliana, A.: Micromechanics models for the effective nonlinear electro-mechanical responses of piezoelectric composites. Acta Mech. **224**, 1471–1492 (2013)
17. Kar-Gupta, R., Venkatesh, T.A.: Electromechanical response of 1–3 piezoelectric composites: effect of poling characteristics. J. Appl. Phys. **98**, 054102 (2005)
18. Kar-Gupta, R., Marcheselli, C., Venkatesh, T.A.: Electromechanical response of 1–3 piezoelectric composites: effect of fiber shape. J. Appl. Phys. **104**, 024105 (2008)
19. Dai, Q., Ng, K.: Investigation of electromechanical properties of piezoelectric structural fiber composites with micromechanics analysis and finite element modeling. Mech. Mater. **53**, 29–46 (2012)
20. Brockmann, T.H.: Theory of Adaptive Fiber Composites: From Piezoelectric Material Behavior to Dynamics of Rotating Structures, vol. 161. Springer, Heidelberg (2009)
21. Most, T., Bucher, C.: New concepts for moving least squares: an interpolating non-singular weighting function and weighted nodal least squares. Eng. Anal. Bound. Elem. **32**, 461–470 (2008)
22. Liu, G.-R., Gu, Y.-T.: An Introduction to Meshfree Methods and Their Programming. Springer, Heidelberg (2005)
23. Dang, T.D., Sankar, B.V.: Meshless local Petrov–Galerkin formulation for problems in composite micromechanics. AIAA J. **45**, 912–921 (2007)
24. Ahmadi, I., Aghdam, M.M.: Micromechanics of fibrous composites subjected to combined shear and thermal loading using a truly meshless method. Comput. Mech. **46**, 387–398 (2010)
25. Ahmadi, I., Aghdam, M.M.: A truly generalized plane strain meshless method for combined normal and shear loading of fibrous composites. Eng. Anal. Bound. Elem. **35**, 395–403 (2011)
26. Belytschko, T., Lu, Y.Y., Gu, L.: Element-free Galerkin methods. Int. J. Numer. Methods Eng. **37**, 229–256 (1994)
27. Dolbow, J., Belytschko, T.: An introduction to programming the meshless element free Galerkin method. Arch. Comput. Methods Eng. **5**, 207–241 (1998)
28. Aghdam, M.M., Pavier, M.J., Smith, D.J.: Micro-mechanics of off-axis loading of metal matrix composites using finite element analysis. Int. J. Solids Struct. **38**, 3905–3925 (2001)
29. Fernández-Méndez, S., Huerta, A.: Imposing essential boundary conditions in mesh-free methods. Comput. Methods Appl. Mech. Eng. **193**, 1257–1275 (2004)
30. Zhu, T., Atluri, S.N.: A modified collocation method and a penalty formulation for enforcing the essential boundary conditions in the element free galerkin method. Comput. Mech. **21**, 211–222 (1998)
31. Tang, T., Yu, W.: Variational asymptotic micromechanics modeling of heterogeneous piezoelectric materials. Mech. Mater. **40**, 812–824 (2008)
32. Liu, G.-R.: Meshfree Methods: Moving Beyond the Finite Element Method. CRC Press, Boca Raton (2009)
33. Amdahl, G.M.: Validity of the single processor approach to achieving large scale computing capabilities. In: Proceedings of the April 18–20, 1967, Spring Joint Computer Conference, pp. 483–485. ACM (1967)
34. Meitzler, A., Tiersten, H.F., Warner, A.W., Berlincourt, D., Couqin, G.A., Welsh III, F.S.: IEEE Standard on Piezoelectricity. ANSI/IEEE Std 176–1987 (1988). doi:10.1109/IEEESTD.1988.79638